Effects of L-arginine concentration on hematite nanostructures synthesized by spray pyrolysis and chemical bath deposition

Justine Sageka Nyarige, Tjaart P. J. Krüger, Mmantsae Diale

Department of Physics, University of Pretoria, Private Bag X20, Hatfield, 0028, South Africa

Abstract

Nanostructured hematite films were synthesized using spray pyrolysis and chemical bath deposition. X-ray diffraction measurements revealed sharp diffraction peaks of (012),(104) and (110), describing corundum hexagonal structure of hematite. Raman spectroscopy confirmed polycrystalline hematite symmetry with two E_g and five A_{1g} vibrational phonon modes. Optical studies reported variation of absorbance as precursor concentration increased. The onset absorbance ranged from 595 nm to 650 nm. Scanning electron microscopy reported the shape transformation of nanoparticles to nanospheres. The average grain size obtained for the nanostructures ranged from 41.0±0.5 nm for pristine film to 6.0±0.5 nm for those synthesized with a $FeCl_3.6H_2O$:L-arginine concentration ratio of 1:3. A photocurrent density of 1.6 x 10^{-3} mA/cm^2 for pristine hematite was produced while, 2.7 x 10^{-3} mA/cm^2, 5.4 x 10^{-3} mA/cm^2, and, 9.8 x 10^{-3} mA/cm^2 current densities were obtained for 1:1, 1:2 and 1:3 $Fe_3.6H_2O$:L-arginine respectively.

Keywords: Hematite, L-arginine, nanostructures, chemical bath deposition

1. Introduction

Solar energy has been widely considered one of the alternative sources in supplementing fossil fuels whose resources are getting limited every day. More solar energy strikes the earth in one hour than the total global demand [1]. Proper utilization of solar energy will have the potential to alleviate environmental issues such as climate change that has resulted from fossil fuel consumption [2]. However, the harvesting of solar energy and its storage have to be cost effective [3]. Photoelectrochemical (PEC) water splitting is one of the methods recently considered in the conversion of renewable energy to other forms [4]. The PEC cell captures solar energy that is used to produce hydrogen from the splitting of water, which is subsequently stored in the form of chemical bonds and can later be used

*Corresponding author

Email address: mmantsae.diale@up.ac.za

as a fuel. Through effective storage, a sustainable hydrogen-based energy economy can therefore be realized by solar water splitting [5]. Since the work of Fujishima and Honda who first used titanium dioxide (an n-type semiconductor) as a photoanode for PEC water splitting, a lot of research has been ongoing to improve the solar-to-hydrogen efficiency [6]. From their findings, n-type semiconductors proved to be good photoanodes, motivating our research on hematite which belongs to the same family. Compared to titanium dioxide, hematite has been considered a more suitable photoanode because of its small indirect band gap of 1.9-2.2 eV that allows superior absorption of solar energy in the visible region [7]. Other desirable properties of hematite include its non-toxicity, relative abundance and photochemical stability in aqueous environments [8]. However, the reported efficiency is far below the predicted solar-to-hydrogen (STH) efficiency of 15 % [2]. This is attributed to a small hole diffusion length of 2-4 nm [9], fast electron-hole recombination [10], low hole mobility (0.1 cm^2 $V^{-1}S^{-1}$) [11] and low oxygen evolution kinetics [12]. Additionally, the energetic positions of the valence and conduction band edges do not conform with O_2/H_2O and H^+/H_2 redox potentials [13]. Therefore, a minimum external bias of 1.23 eV [14] is required for the splitting of water to produce hydrogen according to the hydrogen and oxygen evolution equation, $2H_2O \longrightarrow 2H_2 + O_2$ [15].

Nanostructuring has since been reported as one of the approaches to improve the efficiency of hematite photoanodes. Bassi *et al.* reported 400-500 nm thick films and short diffusion lengths of 5-10 nm are required for complete light absorption and efficient hole transport to the electrolyte [16]. Different nanostructures like cauliflowers [17], nanorods [18, 19], dendritic nanowires [20], and nanotubes [21] have been reported. Nanostructuring enhances the surface area of the films, which further improves the photocurrent production. However, not much information has been reported on the structural, morphological and optical properties of nanospheres for PEC applications. In our previous study, L-arginine, a carboxyllic amino acid, was used to transform the shape of the nanoparticles (NPs) to nanospheres [22]. To the best of our knowledge, L-arginine has not yet been used as a reducing agent in controlling the size of nanospheres. In addition, The strong hydrogen bond makes the arginine soluble in polar molecules and water. Figure 1 shows the structure of L-arginine with the hydrogen bonding on the amine (NH) and hydroxide (OH) part.

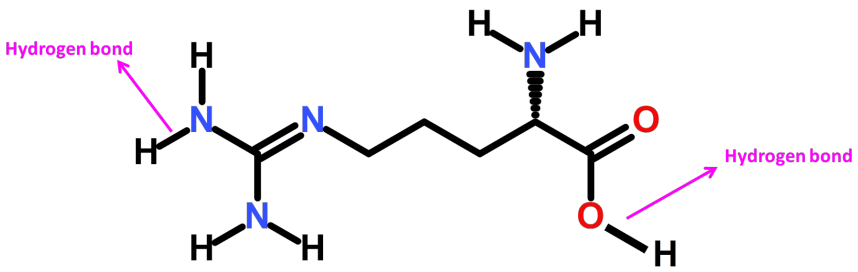

Figure 1: The hydrogen bond in the L-arginine molecular structure.

In this study, hematite NPs were synthesized using spray pyrolysis at a temperature of 430°C. L-arginine was used to transform the shape and size of NPs through chemical bath deposition at a fixed temperature of 90°C for 48 hours. As such, well-defined hematite superstructures with different nanoscale architectures and uniform geometry were obtained. By increasing the surface area the hole diffusion lengths were shortened, thereby reducing the distance that minority charge carriers travel during the diffusion process in PEC applications. Morphological characterization of the hematite nanostructures revealed a high purity and polycrystallinity, with uniform grain sizes ranging from 6.0 to 41.0±0.5 nm. Perfect lattice fringes were confirmed by the crystal growth of (012), which was the dominant diffraction peak in all samples.

2. Experiment

Chemical spray pyrolysis was used in the synthesis of hematite nanostructures using 0.05 M $Fe(NO_3)_3.9H_2O$ (Sigma Aldrich, AR, 99.99 %) as the precursor and fluorine doped tin oxide (Sigma Aldrich, 8Ω/sq). A deposition temperature of 430°C, spray rate of 10 ml/min and deposition height of 30 cm were used. The solution was then sprayed onto a preheated fluorine-doped tin oxide (FTO) substrate using a 1 mm nozzle for 45 seconds. The prepared samples were annealed at 450°C and later used as seed layers for the transformation of NPs into nanospheres by chemical bath deposition (CBD).

CBD was then used to transform the irregularly shaped hematite NPs into nanospheres where L-arginine ($C_6H_{14}N_4O_2$, Sigma Aldrich, reagent grade 98 %), a biomolecule, assisted in the modification process. $Fe(NO_3)_3.9H_2O$:L-arginine mole concentration ratios of 1:1, 1:2 and 1:3, respectively, were prepared in 30 ml deionized water. The mixture ($FeCl_3.6H_2O$ and L-arginine) was thereafter grown on pristine hematite thin films. The experiments were performed at a fixed bath temperature of 90°C while stirring continuously using a magnetic stirrer for 48 hours. The prepared samples were later rinsed in deionized water and ethanol before drying at room temperature for 10 hours. Figure 1 summarizes the process of the NPs synthesis.

Characterization

The morphology of the α-Fe_2O_3 samples was determined using a field emission scanning electron microscope (Zeiss Ultra PLUS FESEM-Microscopes) operating at 2 kV. ImageJ was used in estimating the grain sizes while Gaussian fitting was performed to obtain the frequency of the histogrammed nanoparticle size distribution. X-ray diffraction was used to investigate the crystal structure of the films using a Bruker D2 Phaser X-ray diffractometer (XRD) with CuK_α radiation, a 0.15418 nm source, scanning speed of 0.05° per minute for a 2θ range at 20°-70°. Raman spectroscopy was performed using a WITec alpha300 RAS+ confocal Raman microscope with 532 nm excitation, while the absorbance was measured using a Cary 100 Bio UV-Vis spectrophotometer.

Potentiostat (VersaSTA 3F, U.S.A) was used to measure the current-voltage (I-V) of hematite thin films. The three electrodes were inserted in the Photoelectrochemical ('cappucino') cell with sodium hydroxide (NaoH), pH 13.8 as the electrolyte. Platinum mesh was

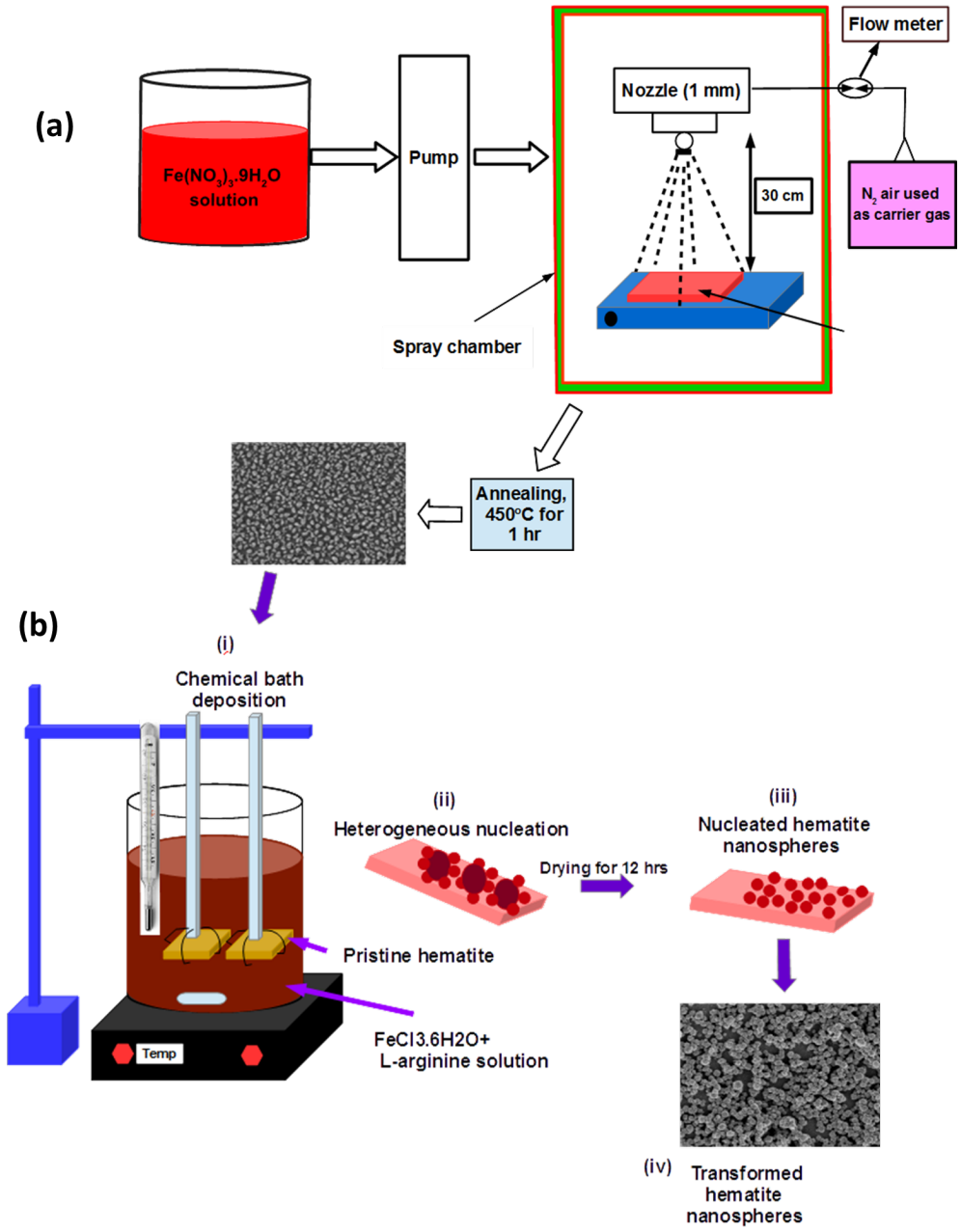

Figure 2: Schematic diagram of spray pyrolysis (a) and chemical bath deposition (b) used for transformation of hematite nanoparticles at a bath temperature of 90°C for 48 hours to nanospheres.

used a counter electrode, 3.0 M KCl saturated Ag/AgCl as reference electrode and hematite photoanode as the working electrode. Both dark and light I-V measurements were performed using a scan rate of 50 mVs^{-1}. Simulated sun (AM 1.5G) was irradiated to hematite photoanode with an area of 0.49 cm^2 using solar simulator (Newport LSC 100 W Xenon lamp). The detector (Newport) was used to adjust the light intensity to 100 Wcm^{-2}. Finally, the

obtained potentials were converted to reversible hydrogen electrode (RHE) using the Nernst equation 1 [23]:

$$E_{RHE} = E_{(Ag/AgCl)} + 0.059PH + E^{\circ}_{(Ag/AgCl)} \quad (1)$$

where $E^{\circ}_{(Ag/AgCl)}$ is 0.205 V at 25°, and $E_{(Ag/AgCl)}$ is the potential against reference electrode (Ag/AgCl) measured experimentally.

3. Results and Discussion

Iron oxhydrate was formed during spray pyrolysis synthesis at 430°C. The films were transferred to the furnace and annealed at 450°C for one hour to obtain hematite according to the following reaction [24]:

$$4Fe(NO_3)_3.9H_2O \longrightarrow 2Fe_2O_3 + 12NO_2 + 21H_2 + 15H_2O \quad (2)$$

3.1. Structural properties

Figure 3 shows the X-ray diffraction patterns of all hematite films for 2θ ranging from 20° to 70°. Hematite diffraction peaks were indexed at their right 2θ positions. The Miller indices of (104) and (110) indexed according to rhombohedral hexagonal α-Fe_2O_3 at 33.3° and 35.5°, respectively, were the dominant peaks. The peaks are associated with a corundum structure of hematite with space group $R^{-}3C$ and were used to calculate the lattice constants using equations 3 and 4 [25].

$$2d_{hkl}sin\theta = n\lambda, \quad (3)$$

and

$$\frac{1}{d^2_{hkl}} = \frac{4}{3a^2}(h^2 + k^2 + hk) + \frac{l^2}{c^2}, \quad (4)$$

The average lattice constants, a = b (for hexagonal crystal structure) and c obtained were 5.021 $^{\circ}A$and 13.524 $^{\circ}A$ respectively. The obtained lattice constants were similar to a, b = 5.0356 and c = 13.7489 (JCPDS file Card, No 33-0664) [26]. Additionally, the strong, sharp diffraction peaks confirm well-crystallized hematite films. Moreover, the (012) diffrac-tion peak at 25.6° was dominated the other peaks, confirming the perfect lattice fringes of hematite. No diffraction peaks for other phases of iron oxide were observed, confirming further purity of the hematite films. Dominant peaks of fluorine-doped tin oxide (SnO_2:F) were also identified. Similar results were obtained by Marin *et al.* and Rao *et al.* on the growth of hematite nanoparticles using a hydrothermal technique for gas sensing [27, 28].

The crystallite size of hematite and L-arginine/hematite nanostructures and nanospheres were obtained from Debye Scherrer's equation [29]:

$$D = \frac{0.9\lambda}{\beta \cos\theta}, \quad (5)$$

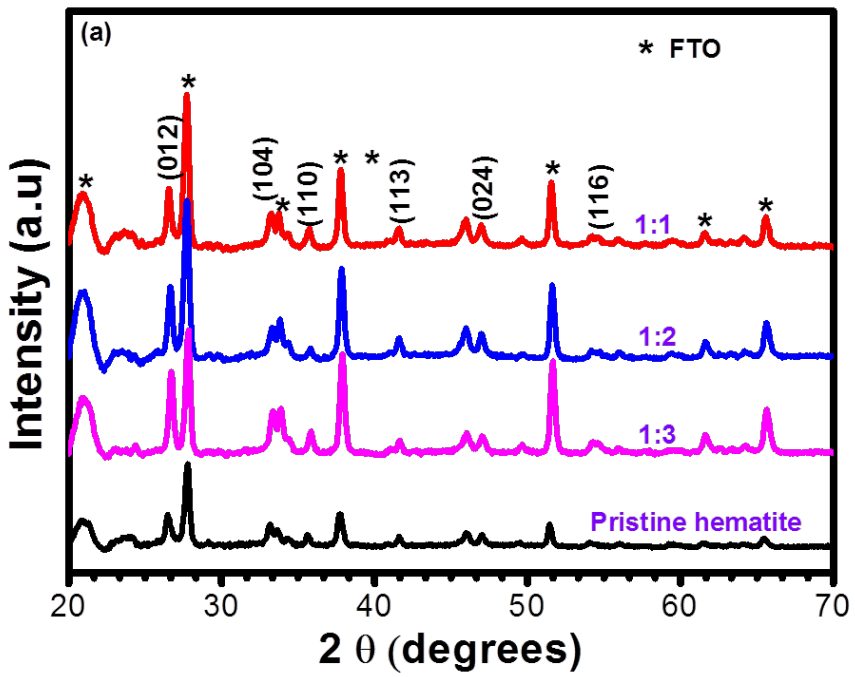

Figure 3: XRD spectra of hematite nanostructures synthesized by spray pyrolysis at 430°C and L-arginine/hematite films prepared by CBD for different $FeCl_3.6H_2O$:L-arginine concentrations of 1:1, 1:2, 1:3.

where λ is the wavelength of the X-ray beam and β is the full-width at half-maximum (FWHM). The change in particle size at different 2θ angles for L-arginine concentration could be due to a change in the geometrical shape of the nanospheres.

As the Bragg angle increased, FWHM increased non-linearly with a decrease in crystallite size, as shown in figure 4. This might have been caused by a finite crystal size at large angles, defects, microstrain and dislocations that took place during the synthesis and annealing processes [30]. Broadening of the peaks at large Bragg angles could also be a result of a non-linear relationship between the d-spacing and the angular aperture of the detector.

The Williamson-Hall model was used to calculate the microstrain (ε), using the following relationship [31]:

$$\varepsilon = \frac{\beta}{4\sin\theta}, \tag{6}$$

The defects in our samples were obtained by the dislocation density equation, given by [32]

$$\delta = \frac{1}{D^2}. \tag{7}$$

The dislocation density and microstrain increased as the $FeCl_3.6H_2O$:L-arginine concentration ratio was varied from 1:1 to 1:3, as summarized in Table 1. A high dislocation

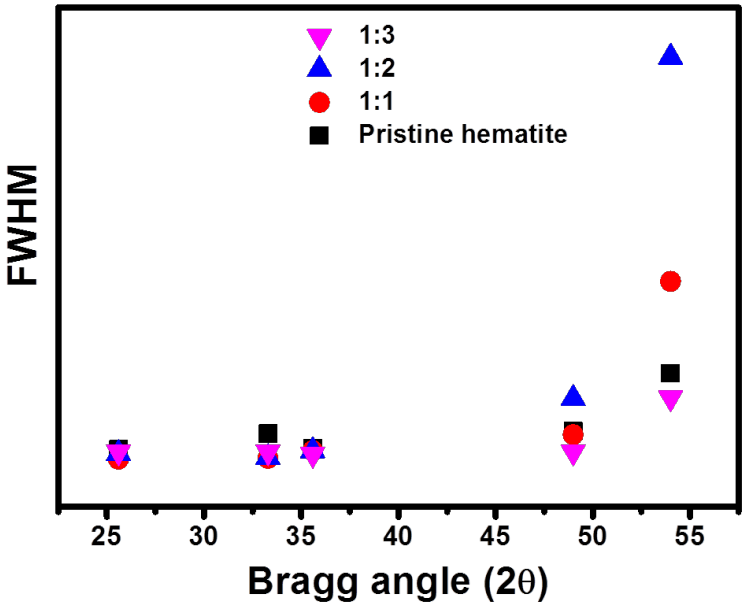

Figure 4: Variation of FWHM and Bragg angles for hematite and L-arginine/hematite nanostructures prepared by chemical spray pyrolysis and chemical bath deposition.

Table 1: Dislocation density and microstrain of hematite and L-arginine/hematite nanostructures

Sample	Average crystal size (nm)	Dislocation density (x 10^{-4} nm)$^{-2}$	Microstrain (x 10^{-4})
Pristine	25.02	1.60	1.73
1:1	31.67	1.10	1.44
1:2	29.43	1.16	1.61
1:3	28.79	1.21	1.67

density of 1.60 x 10^{-4} nm^{-2} on pristine hematite could the result of imperfections and stacking faults of different layers during synthesis. Additionally, as the L-arginine concentration was increased with respect to $FeCl_3.6H_2O$ from a ratio of 1:1 to 3:1, the dislocation density increased from 1.10 x 10 $^{-4}$ nm^{-2} to 1.21 x 10^{-4} nm^{-2} (see Table 1). This could be caused by locking of the effective stress as oxygen diffused during the nanoparticle transformation process. Similar results have been reported by Tomoro *et al.* on the effect of oxygen concentration in silicon crystals during direct solidification [33].

Raman spectroscopy was used to further determine the crystallinity and phonon modes of hematite using green laser light at 532 nm. Equation 7 presents the vibrational modes in the first Brillouin zone [34]:

$$\Gamma_{vib} = 2A_{1g} + 2A_{1u} + 3A_{2g} + 2A_{2u} + 5E_g + 4E_u. \tag{8}$$

where A_{1g}, A_{1u}, A_{2g}, A_{2u}, E_g and E_u are the irreducible representation for the optical modes of hematite structure [35].

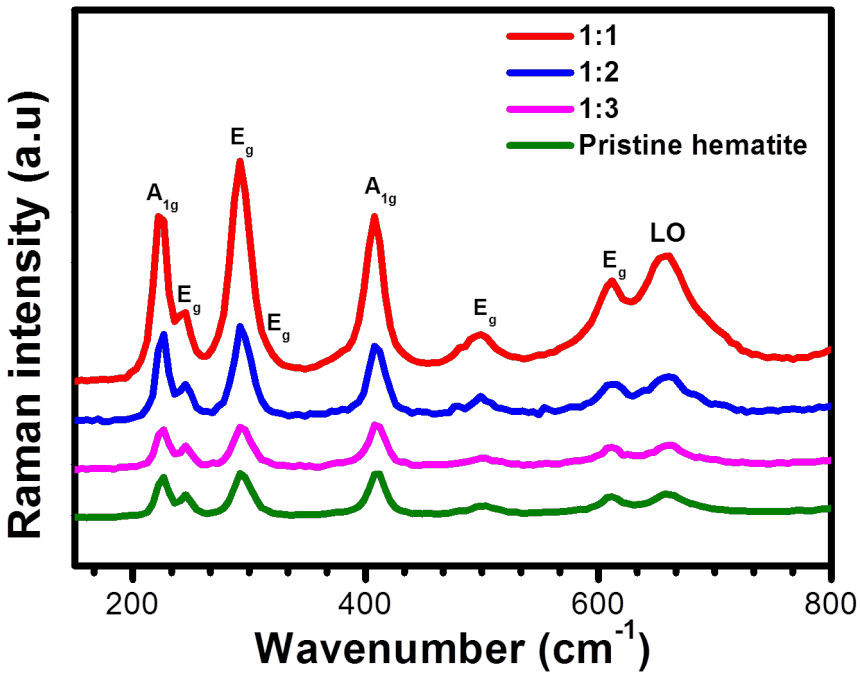

Figure 5: Raman spectroscopy of hematite and L-arginine/hematite nanostructures prepared by spray pyrolysis and CBD at 1:1, 1:2 and 1:3 $FeCl_3.6H_2O$:L-arginine concentrations.

Symmetrical phonon modes of hematite, which are Raman active, were observed in all the samples. From figure 5, the peaks at 243 cm^{-1} and 409 cm^{-1} were associated with the A_{1g} phonon mode, while the 226 cm^{-1}, 240 cm^{-1}, 293 cm^{-1}, 500 cm^{-1} and 609 cm^{-1} peaks were assigned to E_g vibrations. The 656 cm^{-1} peak (LO), whose intensity was increasing with deposition, was due to the ferromagnetic properties of hematite. High intensity peaks were observed for the 1:1 L-arginine/hematite film, which may be due to equimolar interactions of the carbon and hydrogen bonds, leading to uniform vibrational modes. Raman peaks of L-arginine were not present in all samples, which further confirms the purity of the hematite nanostructures.

3.2. Morphology and elemental analysis

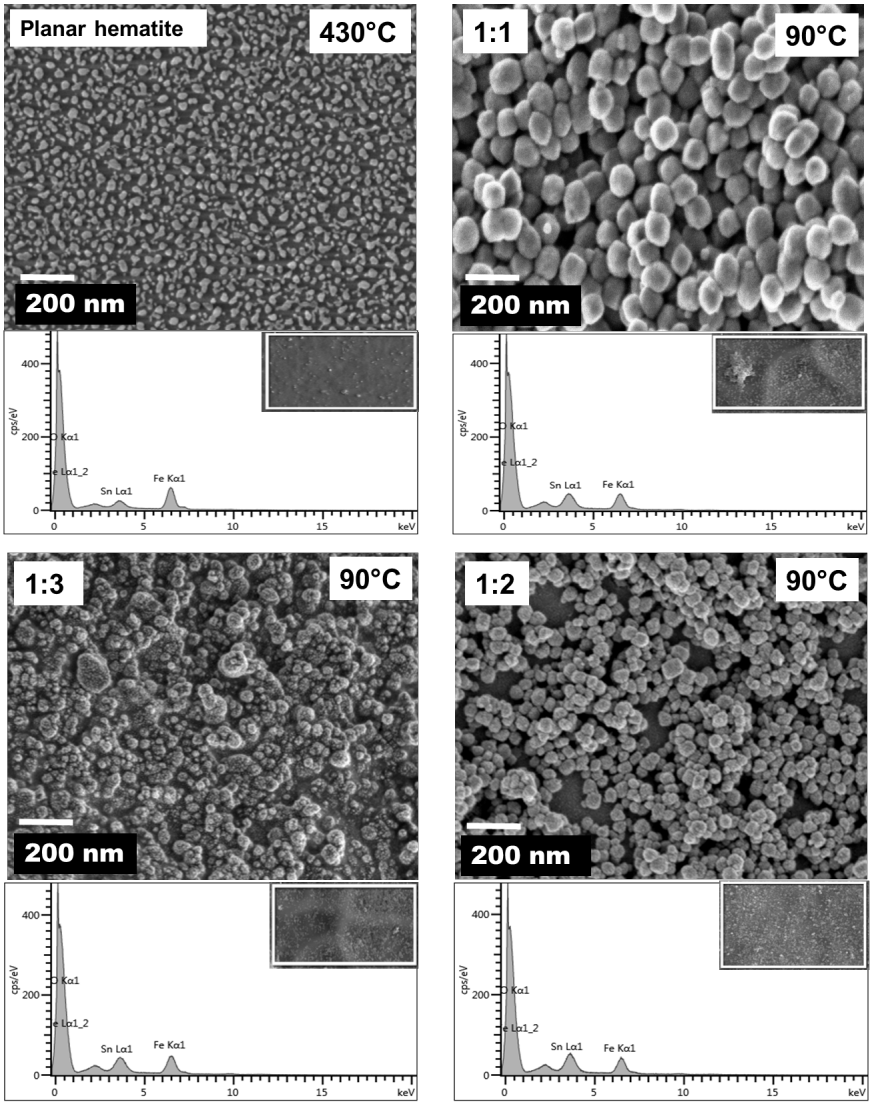

Figure 6: FESEM surface morphology of hematite and L-arginine/hematite nanostructures synthesized by spray pyrolysis at 430 °C and CBD at a fixed temperature of 90 °C for 48 hours. Below the morphology of each sample are the EDX spectra showing elemental composition of each sample.

The synthesized hematite films had a uniform nanoporous morphology with an average grain size of 41.0±0.5 nm, as shown in figure 6. After treatment of NPs with L-arginine through CBD, the irregularly shaped NPs were transformed into uniform spherical nanospheres, evenly distributed on the sample. The uniform growth of the nanospheres was enhanced by the hydrogen bond between the -NH_2 and -COOH functional groups of L-arginine and $FeCl_3.6H_2O$, signifying strong interactions. Figure 7 shows the variation of the grain size as the molar concentration ratio was increased from 1:1 to 1:3 for $FeCl_3.6H_2O$:L-arginine, obtained from ImageJ, Gaussian fitting and histogram. The grain sizes were ob-

served to decrease as the L-arginine concentration increased, averaged at 35.0 ±0.5 nm, 6.0±0.5 nm, and 8.0±0.5 nm, for concentration ratios of 1:1, 1:2, and 1:3, respectively. The decrease in the grain size could be due to suppressed growth of geothite (βFOOH), the unstable phase of iron oxide which later transforms to stable α-Fe_2O_3. These changes could also be due to the high rate of heterogeneous nucleation on the hematite seeded layer. The grains were, however, not similar in size with crystallite sizes obtained by XRD but report the general trend as expected. This is largely due to the Scherrer formula used for XRD that is different from absolute measured FESEM. Grain size reduction could also be the result of microstrains and the presence of other defects. This is evidenced by peak broadening at large 2θ angles.

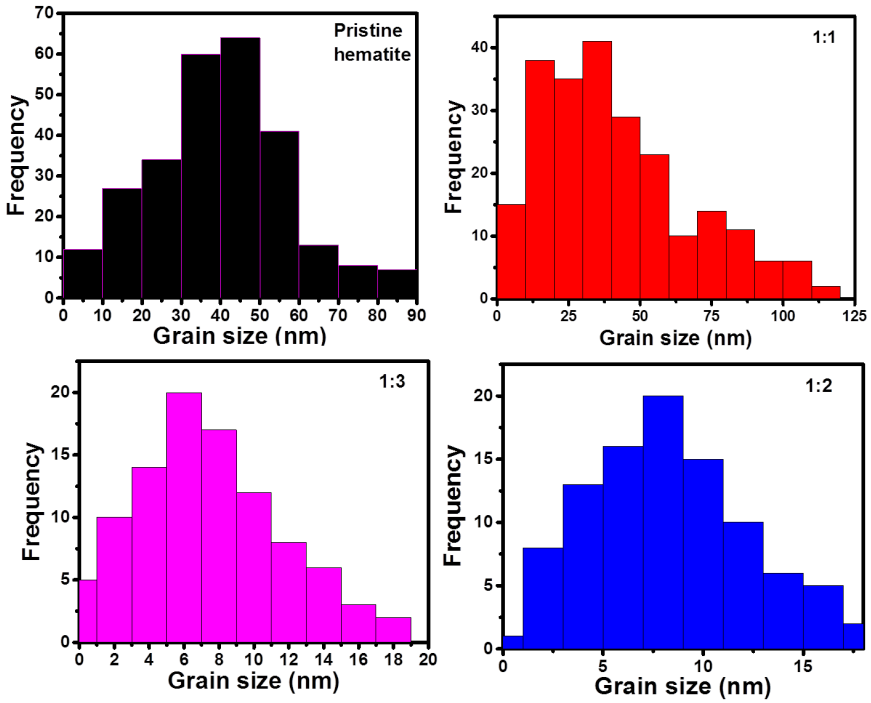

Figure 7: Grain size distribution of hematite and L-arginine/hematite nanostructures prepared by thermal spray pyrolysis and CBD.

EDX was used to calculate the elemental composition and stoichiometry of the synthesized films. The EDX spectra are shown in figure 6, at the bottom of surface morphology images. Predominant signals of iron (Fe) and oxygen (O) were reported by Frydrych *et al.* [36]. The line at 6.42 keV represents the K-line of iron (Fe), while the K-line of oxygen (O) was observed at 0.53 eV, in agreement with previous reports [36]. However, there was L line which was observed close to the K line for oxygen for all the samples. This could be associated with the oxygen composition since it was predominant in all the samples. The L shell further could have split into 1 and 2 so as to accommodate the population of oxy-gen composition in hematite and L-arginine/hematite films [37]. The other spectral peaks originate from tin (Sn), which was used as the substrate. Figure 8 shows the weight percentage composition of Fe

and O that form hematite at different concentrations. No other elements were identified by EDX, thus confirming the purity of the nanostructures. The percentage of the elements was varied slightly depending on the concentration. The EDX results, therefore, confirm the purity of the hematite nanostructures and are in good agree-ment with the structural properties reported in sections 3.1 and 3.2. Ubale *et al.* reported similar results using a Successive Ionic Layer Adsorption and Reaction (SILAR) method to synthesize nanocrystalline hematite [38].

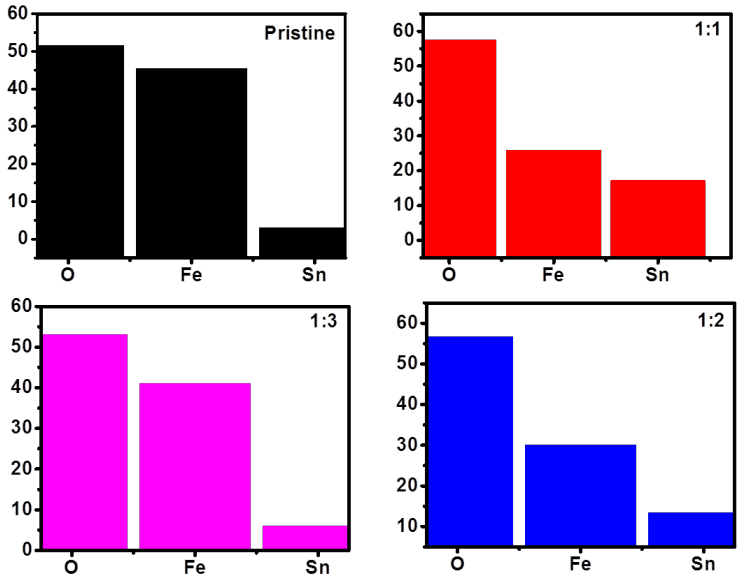

Figure 8: EDX histogram by wt % of hematite NPs prepared by spray pyrolysis at 430 °C, L-arginine/hematite NPs prepared by CBD at a bath temperature of 90 °C for 48 hours for $FeCl_3.6H_2O$:L-arginine concentrations of 1:1, 1:2, and 1:3, respectively.

3.3. Optical properties

UV-Vis spectroscopy was used to measure the absorbance of the nanostructured films. Figure 9 indicates an observable blue-shift in absorbance with increasing L-arginine concentration. The absorption is almost linear in the red region of the electromagnetic spectrum. The nanocrystalline absorption band edge of hematite ranged from 595 to 650 nm, with d-d being the main transition in this region, less charge transfer and the pair excitation [29]. All the samples revealed high absorption in the visible region with the absorption tail extending to beyond 670 nm. The band gap of the hematite nanostructures was estimated by extrapolation of the tangent line at the onset of the absorbance. From the estimation, the band gap values were 1.91 eV for pristine hematite, and 1.96 eV, 2.04 eV, and 2.08 eV for $FeCl_3.6H_2O$:L-arginine ratios of 1:1, 1:2, and 1:3, respectively. The estimated band gap has been reported by other researchers using absorbance and Tauc plot models [39, 40]. The growth of L-arginine on hematite NPs had no much effect on the electron movements since the

indirect transitions from valence band to Fe^{3+} d orbitals was still maintained [41]. In addition, although the d-d transitions are both spin and partly forbidden, they some-times occur with a finite transition and become allowed through other means like magnetic coupling of electronic spins nearer to Fe^{3+} of the hematite crystals [42].

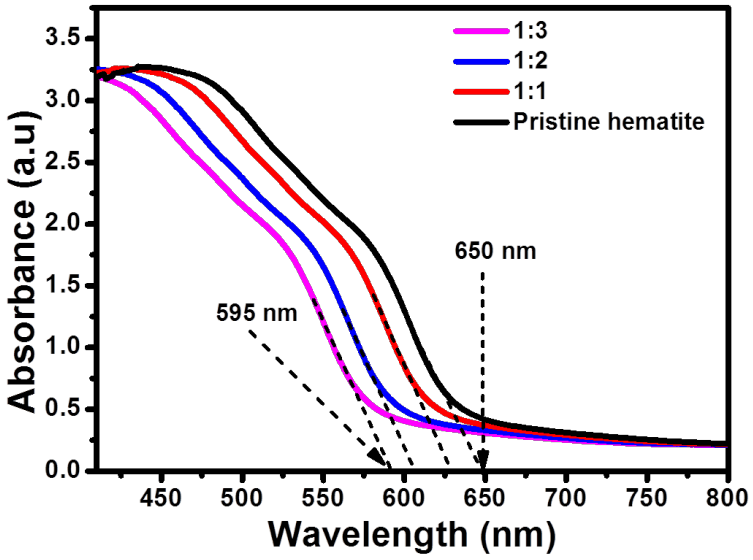

Figure 9: Variation of absorbance of hematite films prepared by spray pyrolysis at 430°C and 1:1, 1:2, and 1:3 $FeCl_3.6H_2O$:L-arginine, respectively, prepared by CBD at a bath temperature of 90°C

3.4. Photocurrent measurements

The current density for all the films were measured using using the potentiostat (Versa-STAT 3, U.S.A) under 1.5 G solar light radiations as discussed in section 2. The pristine hematite film recorded a low current density of 1.6 x 10^{-3} mA/cm^2 at 1.23 V vs. RHE. For $FeCl_3.6H_2O$:L-arginine films, 2.7 x 10^{-3} mA/cm^2, 5.4 x 10^{-3} mA/cm^2, 9.8 x 10^{-3} mA/cm^2 current densities at 1.23 V vs. RHE were measured. This was a significant increase from the pristine hematite NPs. This change in the current densities could be attribute to the transformation of the grain size from nanoparticles to nanospheres. The L-arginine which was used as a reducing agent played a big role in the increase in the current densities. In addition, there was a shift in the photocurrent onset for 1:2 and 1:3 of $FeCl_3.6H_2O$:L-arginine respectively films to 0.90 mV. Bora *et al.* [43] have reported a comparable results where L-arginine was used as a transformative agent using hydrothermal synthesis to obtain hematite nanorods, with the highest photocurrent density of 2.18 x 10^{-3} mA/cm^2 at 450 mV vs. Ag/AgCl.

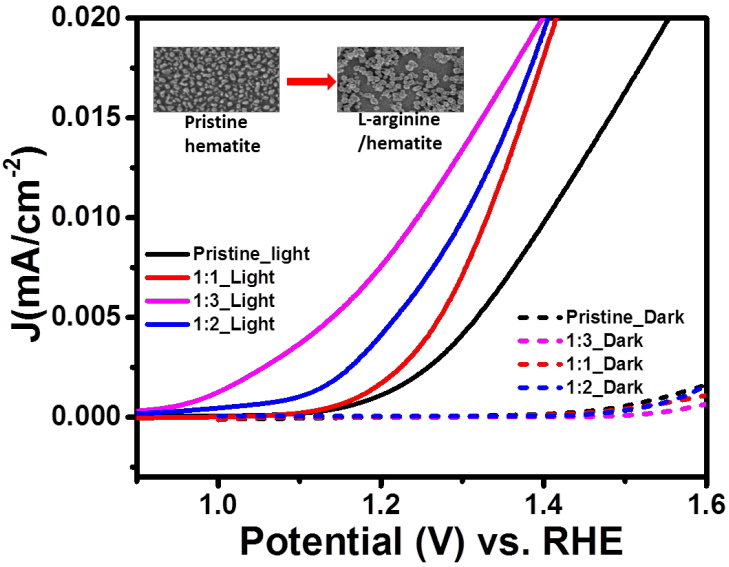

Figure 10: Photocurrent density curves for pristine and L-arginine/hematite nanostructures for 1:1, 1:2 and 1:3 of $FeCl_3.6H_2O$:L-arginine precursor concentrations respectively, prepared by spray pyrolysis (pristine) and CBD (L-arginine/hematite films). The scan rate is 50 mVs^{-1} with 1 M NaOH as electolyte.

4. Conclusion

We presented hematite nanospheres on an FTO substrate by varying the relative concentration of $FeCl_3.6H_2O$ and L-arginine. XRD results confirmed the corundum hexagonal structure with characteristic peaks at (012), (104), and (110), indexed at 25.6°, 33.3° and 35.5°, respectively. Raman spectroscopy studies revealed two E_g and five A_{1g} sharp, symmetrical vibrational phonon modes. FESEM revealed irregular and uniform shapes of hematite nanostructures synthesized by spray pyrolysis and chemical bath deposition, respectively. The grain sizes were observed to decrease from 41.0±0.5 nm for pristine hematite to 6.0±0.5 nm for 1:3 $FeCl_3.6H_2O$:L-arginine. The onset absorbance of the films ranged between 595 and 650 nm with an energy band gap estimation of 1.91-2.08 eV. A photocurrent density of 1.6 x 10^{-2} mA/cm^2 for pristine hematite was produced while 2.7 x 10^{-3} mA/cm^2, 5.4 x 10^2 mA/cm^2 and 9.8 x 10^{-3} mA/cm^2 current densities at 1.23 V vs. RHE were obtained for 1:1, 1:2 and 1:3 $Fe_3.6H_2O$:L-arginine respectively. In conclusion, the L-arginine has reported to improve the amount of photocurrent produced significantly. This was enhanced by the small grain sizes obtained, good absorption in the visible region and polycrystallinity of these nanostructures.

Acknowledgement

The authors wish to thank the Department of Physics, University of Pretoria for support, the African Laser Centre (ALC, J.S.N.) and the National Research Foundation (NRF) grant No. N0115/115463 (SARChI, M.D.), and grant No. N00500/112085 (T.P.J.K.) for financial support.

References

[1] B. Iandolo, B. Wickman, I. Zorić, A. Hellman, Journal of Materials Chemistry A **3** (2015) 16896–16912.
[2] A. G. Tamirat, J. Rick, A. A. Dubale, W.-N. Su, B.-J. Hwang, Nanoscale Horizons **1** (2016) 243–267.
[3] A. A. Yadav, Journal of Materials Science: Materials in Electronics **27** (2016) 12876–12883.
[4] P. Babar, B. Pawar, A. Lokhande, M. Gang, J. Jang, M. Suryawanshi, S. Pawar, J. H. Kim, Journal of energy chemistry **26** (2017) 757–761.
[5] K. Sivula, F. Le Formal, M. Grätzel, ChemSusChem **4** (2011) 432–449.
[6] A. Fujishima, K. Honda, nature **238** (1972) 37.
[7] Y. Liu, Y.-X. Yu, W.-D. Zhang, Electrochimica Acta **59** (2012) 121–127.
[8] Y. Qiu, S.-F. Leung, Q. Zhang, B. Hua, Q. Lin, Z. Wei, K.-H. Tsui, Y. Zhang, S. Yang, Z. Fan, Nano letters **14** (2014) 2123–2129.
[9] F. L. Souza, K. P. Lopes, E. Longo, E. R. Leite, Physical Chemistry Chemical Physics **11** (2009) 1215–1219.
[10] N. J. Cherepy, D. B. Liston, J. A. Lovejoy, H. Deng, J. Z. Zhang, The Journal of Physical Chemistry B **102** (1998) 770–776.
[11] C. Y. Cummings, F. Marken, L. M. Peter, K. Upul Wijayantha, A. A. Tahir, Journal of the American Chemical Society **134** (2011) 1228–1234.
[12] A. J. Abel, I. Garcia-Torregrosa, A. M. Patel, B. Opasanont, J. B. Baxter, The Journal of Physical Chemistry C **119** (2015) 4454–4465.
[13] N. Dalle Carbonare, V. Cristino, S. Berardi, S. Carli, R. Argazzi, S. Caramori, L. Meda, A. Tacca, C. A. Bignozzi, ChemPhysChem **15** (2014) 1164–1174.
[14] M. G. Walter, E. L. Warren, J. R. McKone, S. W. Boettcher, Q. Mi, E. A. Santori, N. S. Lewis, Chemical reviews **110** (2010) 6446–6473.
[15] R. Li, Y. Weng, X. Zhou, X. Wang, Y. Mi, R. Chong, H. Han, C. Li, Energy & Environmental Science **8** (2015) 2377–2382.
[16] P. S. Bassi, L. H. Wong, J. Barber, et al., Physical Chemistry Chemical Physics **16** (2014) 11834–11842.
[17] A. Kay, I. Cesar, M. Grätzel, Journal of the American Chemical Society **128** (2006) 15714–15721.
[18] H. Mulmudi, N. Mathews, X. Dou, L. Xi, S. Pramana, Y. Lam, S. Mhaisalkar, Electrochemistry Communications **13** (2011) 951–954.
[19] L. Xi, P. D. Tran, S. Y. Chiam, P. S. Bassi, W. F. Mak, H. K. Mulmudi, S. K. Batabyal, J. Barber, J. S. C. Loo, L. H. Wong, The Journal of Physical Chemistry C **116** (2012) 13884–13889.
[20] J. Y. Zheng, M. J. Kang, G. Song, S. I. Son, S. P. Suh, C. W. Kim, Y. S. Kang, CrystEngComm **14** (2012) 6957–6961.
[21] L. Chen, H. Xu, L. Li, F. Wu, J. Yang, Y. Qian, Journal of Power Sources **245** (2014) 429–435.
[22] J. Nyarige, T. P. Krüger, M. Diale, Applied surface and interface: Nanosmat 2018 conference proceeding (2019,submitted).
[23] E. S. Cho, M. J. Kang, Y. S. Kang, Physical Chemistry Chemical Physics **17** (2015) 16145–16150.
[24] A. S. Hassanien, A. A. Akl, Applied Physics A **124** (2018) 752.
[25] Y. Meftah, D. Bekker, B. Benhaoua, A. Rahal, A. Benhaoua, A. Hamzaoui, Digest Journal of Nanomaterials and Biostructures **13** (2018) 465–474.
[26] X. Liu, G. Qiu, A. Yan, Z. Wang, X. Li, Journal of alloys and compounds **433** (2007) 216–220.
[27] X. Rao, X. Su, C. Yang, J. Wang, X. Zhen, D. Ling, CrystEngComm **15** (2013) 7250–7256.
[28] M. Tadić, N. Čitaković, M. Panjan, Z. Stojanović, D. Marković, V. Spasojević, Journal of alloys and compounds **509** (2011) 7639–7644.
[29] S. Shinde, R. Bansode, C. Bhosale, K. Rajpure, Journal of Semiconductors **32** (2011) 013001.
[30] M. Somaraj, N. John, N. J. Tharayil, S. Usha, in: IOP Conference Series: Materials Science and Engineering, volume **360**, IOP Publishing, p. 012017.
[31] M. L. Meier, Department of Chemical Engineering and Materials Science, University of California (2005).
[32] J. Ayers, Journal of Crystal Growth **135** (1994) 71–77.
[33] T. Ide, H. Harada, Y. Miyamura, M. Imai, S. Nakano, K. Kakimoto, Crystals **8** (2018) 244.

[34] A. M. Jubb, H. C. Allen, ACS Applied Materials & Interfaces **2** (2010) 2804–2812.
[35] S. Porto, R. Krishnan, The Journal of Chemical Physics **47** (1967) 1009–1012.
[36] J. Frydrych, L. Machala, M. Hermanek, I. Medrik, M. Mashlan, J. Tucek, J. Pechousek, V. K. Sharma, Thin Solid Films **518** (2010) 5916–5919.
[37] D. E. Newbury*, N. W. Ritchie, Scanning **3**5 (2013) 141–168.
[38] A. Ubale, M. Belkhedkar, Journal of Materials Science & Technology **31** (2015) 1–9.
[39] S. Piccinin, Physical Chemistry Chemical Physics **21** (2019) 2957–2967.
[40] S. Y. Chiam, M. H. Kumar, P. S. Bassi, H. L. Seng, J. Barber, L. H. Wong, ACS applied materials & interfaces **6** (2014) 5852–5859.
[41] S. Shen, S. A. Lindley, X. Chen, J. Z. Zhang, Energy & Environmental Science **9** (2016) 2744–2775.
[42] D. M. Sherman, Physics and Chemistry of Minerals **1**2 (????).
[43] D. K. Bora, A. Braun, R. Erni, G. Fortunato, T. Graule, E. C. Constable, Chem. Mater. **23** (2011) 2051–2061.